Journal of Systems Engineering and Electronics
Vol. 34, No. 1, February 2023, pp.1 – 8

Coherent change detection of fine traces based on multi-angle SAR observations

KOU Xiuli[1,2], WANG Guanyong[2], LI Jun[2], and CHEN Jie[1,*]

1. School of Electronics and Information Engineering, Beihang University, Beijing 100191, China;
2. Beijing Institute of Radio Measurement, Beijing 100854, China

Abstract: Coherent change detection (CCD) is an effective method to detect subtle scene changes that occur between temporal synthetic aperture radar (SAR) observations. Most coherence estimators are obtained from a Hermitian product based on local statistics. Increasing the number of samples in the local window can improve the estimation bias, but cause the loss of the estimated images spatial resolution. The limitations of these estimators lead to unclear contour of the disturbed region, and even the omission of fine change targets. In this paper, a CCD approach is proposed to detect fine scene changes from multi-temporal and multi-angle SAR image pairs. Multi-angle CCD estimator can improve the contrast between the change target and the background clutter by jointly accumulating single-angle alternative estimator results without further loss of image resolution. The sensitivity of detection performance to image quantity and angle interval is analyzed. Theoretical analysis and experimental results verify the performance of the proposed algorithm.

Keywords: coherent change detection (CCD), multi-angle, synthetic aperture radar (SAR).

DOI: 10.23919/JSEE.2023.000001

1. Introduction

As an important application of synthetic aperture radar (SAR), change detection [1] is a process that analyzes a pair of remote sensing images acquired on the same geographical area at different times in order to identify changes that may have occurred between the considered acquisition dates [2,3]. Traditional change detection is widely used in disaster assessment [4], agricultural monitoring [5] and other applications [6]. Generally, the "change of interest" is significantly relative to the radar resolution. However, in reconnaissance applications, subtle and weak changes such as vehicle track or footprints need to be detected [7]. Their edge, shape, and intensity information are submerged by the strong clutter environment, making it difficult to be detected by the image-based target recognition or change detection algorithm.

Coherent change detection (CCD) [8−10] is an effective strategy for fine traces detection, which takes advantage of the coherent phase information between images. A majority of coherence estimators are investigated based on local statistics and therefore affect the spatial resolution while few estimators achieve this goal without a significant loss of resolution. The traditional coherence estimator [11−13] for SAR imagery is biased, particularly when the true coherence is low. An alternative estimator was analyzed by Berger [14] under the assumption of equal population variances, which improves the estimation bias. A generalized likelihood ratio test (GLRT) [15] technology is proposed to measure change by incorporating noise in detection statistic in order to handle areas of low signal to noise ratio (SNR). These estimation approaches are direct applications of the spatial stationarity principle. The limitation of these techniques comes from the loss of resolution on the estimated images, which leads to unclear contour of the disturbed region, and even cause the omission of fine change targets. The above problems can be solved by using more multidimensional information of the estimated images. The nonlocal (NL)[16,17] coherence estimator [18] averages pixel values far apart in the image depending on the surrounding patch similarity. This patch-based estimator can preserve the local heterogeneity caused by edges and textures. The multi-pass CCD estimator [19] accumulates the detection statistic in the changed region by jointly processing multiple SAR images of the same route, which reduces the false alarm rate significantly. Novak [20] demonstrated that, as the number of navigations increases, the detection statistic gets accumulated, leading to an improve-

Manuscript received June 26, 2022.
*Corresponding author.

ment of the detection performance [21]. However, effective multi-pass image acquisition brings great challenges to accurate flight path and complex registration, which limits its practical application.

In fact, SAR images are very sensitive to the observation angle due to their unique imaging mechanism [22]. Multi-angle technology [23] is known to improve target recognition accuracy effectively by jointly using multi-view images of the same target [24]. Similarly, the omni-directional scattering characteristic of fine changes in the scene is reflected in multiple images from different directions. The combined use of multi-view images in SAR CCD can give a complete description of the change target and reduce the influence of layover, perspective, shadows, and other phenomena [25,26]. In addition, compared with multi-pass CCD, multi-angle image pairs are easier to be acquired by a heterogeneous radar sensor networks or sub-aperture of spotlight SAR or circular SAR.

In this paper, a multi-angle SAR CCD method is proposed. The multi-angle coherence estimator is investigated by jointly accumulating single-angle alternative estimator results. At the beginning, the multi-angle mathematical model of the difference images supported by multi-angle imaging is derived. Then, the difference image of a certain observation angle is obtained by using alternative coherence estimator. After geographical correction and registration, difference images are integrated to conduct an incoherent composed detector. The performance of the composed estimator is compared with single-angle estimators by the receiver operating characteristic (ROC) curve. The sensitivity of detection performance to image quantity and angle interval is analyzed by near-field data acquired from the electromagnetic spectrum platform. The contribution of this paper is given as follows. Firstly, compared to the single-angle estimator, multi-angle estimator accumulates the detection results from different perspectives to obtain a complete description of fine traces contour. Secondly, false alarms can be reduced by clutter incoherent accumulation. The contrast between the change target and the background clutter can be enhanced without a significant loss of resolution, which is more beneficial to detecting fine traces under low SNR.

This paper is organized as follows. Section 2 shows the model of multi-angle SAR complex images. A description of multi-angle SAR CCD method is presented in Section 3. In Section 4, electromagnetic spectrum experiments and outfield experiments show the effectiveness of the improved detection method. Finally, Section 5 summarizes this paper.

2. Coherence change statistical analysis

2.1 Multi-angle model

The multi-angle model in stripmap SAR is shown in Fig. 1. The platform flies around the target scene region of interest (ROI), with the radar always being side-looking to illuminate the central scene. A set of difference images can be generated by temporal complex SAR image pairs acquired from the same flight route. The slant range of different flights is denoted by R_n (n denotes the flight number), the incident angle is denoted by φ_n, the azimuth angle is denoted by θ_n, and the beam phase center between one flight to another is denoted by θ_{interval} ([0°,180°]), and the quantity of flights to be composed is denoted by N_{compose}.

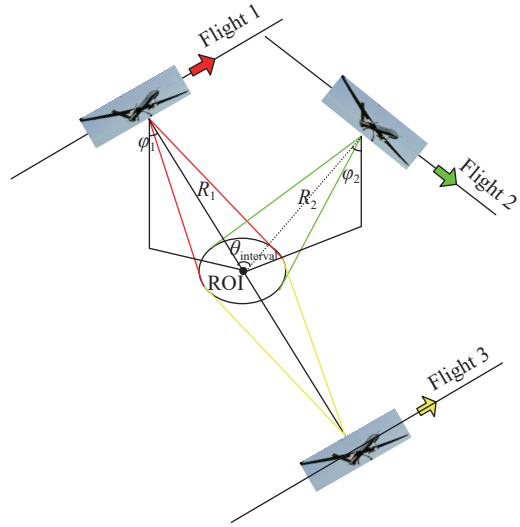

Fig. 1 Multi-angle model

2.2 Sample coherence change statistic

In a repeat pass interferometric SAR collection, it can be shown that under certain conditions [27], the joint distribution of the complex interferometric image pair $\boldsymbol{X} = [f, g]^{\mathrm{T}}$ is a jointly circular, zero mean, Gaussian random vector with density function given by

$$p(\boldsymbol{X}) = \frac{1}{\pi^2 |\boldsymbol{Q}|} \exp(-\boldsymbol{X}^{\mathrm{H}} \boldsymbol{Q}^{-1} \boldsymbol{X}) \tag{1}$$

where f and g are the transduced reflectivity in a resolution cell. $\boldsymbol{Q}$ is the covariance matrix of the transduced pixel pair given by

$$\boldsymbol{Q} = \mathrm{E}(\boldsymbol{X}\boldsymbol{X}^{\mathrm{H}}) = \begin{bmatrix} \sigma_f^2 & \sigma_f \sigma_g \rho \exp(\mathrm{j}\Phi) \\ \sigma_f \sigma_g \rho \exp(-\mathrm{j}\Phi) & \sigma_g^2 \end{bmatrix} \tag{2}$$

where $\boldsymbol{X}^{\mathrm{H}}$ is the complex conjugate transpose of $\boldsymbol{X}$, σ_f^2, and σ_g^2 are the mean backscatter power transduced by the

SAR in a pixel for the primary and repeat pass image respectively. $|\boldsymbol{Q}|$ is the determinant of $\boldsymbol{Q}$. The complex cross channel correlated coefficient is denoted by

$$\gamma = \rho \exp(\mathrm{j}\Phi) \tag{3}$$

where ρ is the amplitude of γ. It is a measure of the scene disturbance between the imaging collections [10] , which takes values in the range of 0 to 1. Φ is the interferometric phase, which is determined by the baseline offset between the primary and repeat pass collections and the terrain topography plus any bulk displacement of the scattering scene between the two data collections.

An alternative estimator analyzed by Berger [14] under the assumption of equal population variances was shown to outperform the classical coherence estimator when the two variances are unequal but close [28]. We adopt the alternative estimator to detect the changed regions as the single-angle estimator which is given by

$$\rho_a = \frac{2\left|\sum_{i=1}^{L} f_i g_i^*\right|}{\sum_{i=1}^{L}\left|f_i f_i^*\right|^2 + \sum_{i=1}^{L}\left|g_i g_i^*\right|^2} \tag{4}$$

where ρ_a is based on the sample coherence evaluated over a local neighborhood of L pixels; f_i and g_i are the transduced reflectivities in a resolution cell from repeat pass complex SAR images; * represents their conjugate transpose. The corresponding probability density function of ρ_a for a general repeat-pass image pair with true underlying coherence [29] takes the following form:

$$\begin{aligned} p(\rho_a|\rho, L) &= (2L-1)(1-\rho^2)^L \rho_a \cdot \\ &(1-\rho_a{}^2)^{L-\frac{3}{2}}\, {}_2F_1(L, L+1/2; 1; \rho^2\rho_a{}^2) \end{aligned} \tag{5}$$

where ${}_2F_1$ is the Gauss hypergeometric function. Examples of the distribution of ρ_a for given ρ and L are shown in Fig. 2.

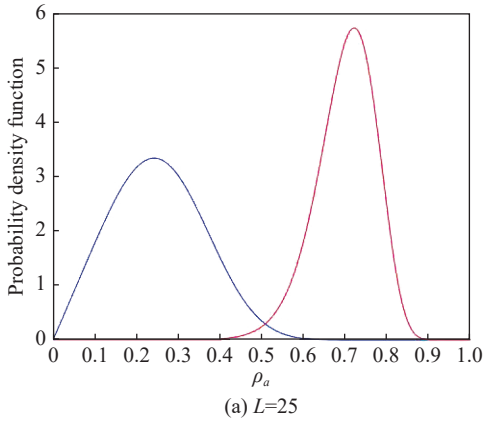

(a) L=25

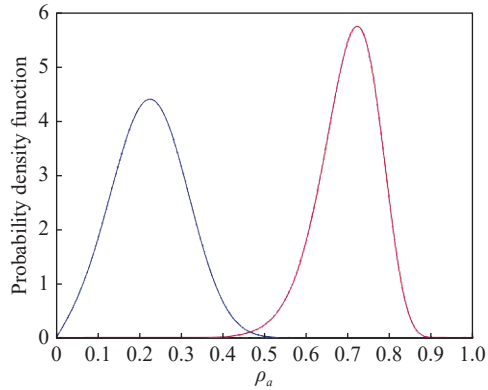

(b) L=49

—— : ρ=0.2; —— : ρ=0.7.

Fig. 2 Sampling distributions of ρ_a shown as a function of sample size L for true parameter values ρ= 0.2 and 0.7

It is shown clearly that, increasing the number of samples in the local window can improve the estimation bias but cause the loss of spatial resolution to the estimated images. The limitation of this estimator leads to unclear contour of disturbed region and even loss of fine change targets. This problem can be solved by using more multi-dimensional information of the estimated images to obtain a complete description of the change target.

3. Method of multi-angle CCD

3.1 Principle of multi-angle CCD

In case of multi-angle imaging, the observed complex interferometric image pair of each angle $[f, g]^{\mathrm{T}}$ is related to platform position [30], which is determined by parameters R_n, φ_n, and θ_n. The corresponding coherence estimator is changed from ρ_a to $\rho_a(n)$, where n represents the observed position.

The assumption here is that the minimum coherence at the angle represents the dominant scattering properties of the change. Under this assumption, we conduct the multi-angle incoherent composed detector using

$$\rho_c = \max_{N_{\mathrm{compose}}} \rho_a'(n)$$

where $\rho_a'(n)$ is the calibrated degree of coherence after geometric correction and registration. It is difficult to obtain the accurate expression for the probability density function of ρ_c. The performance of the composed estimator (we used two angles in this simulation) is compared with single-angle estimator by the ROC curve, which is shown in Fig. 3. For the rationality of this experiment, $\rho = 0$ is chosen to indicate the change and $\rho = 0.9$ to indicate no effective change. Coherence is affected by factors other than scene change, making $\rho = 0.9$ a reasonably high coherence value. Results in detecting change corresponding to $\rho = 0$ versus $\rho = 0.9$ are obtained using 10^4 independent Monte Carlo trials, for sample sizes $L = 25$.

Angle difference between the two observations is 180°. Fig. 3 shows that the performance of the multi-angle CCD method exceeds the single-angle method. Focusing on the red curve, we find that even though probability of false alarm (PFA) is about 0.2, probability of detection (PD) is still as high as 0.9. However, the single-angle method is not able to provide a fine PD even if its PFA is at an unacceptable value of 0.5.

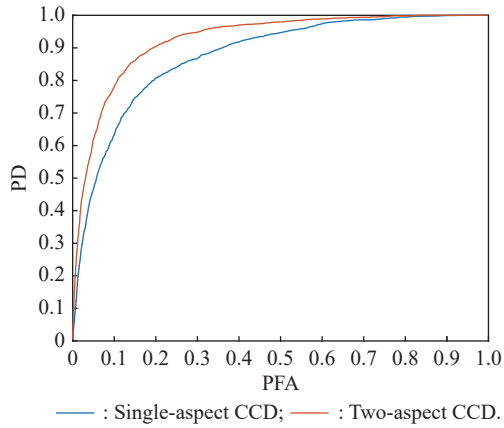

Fig. 3 ROC of multi-angle CCD and single-angle CCD

3.2 Flowchart of multi-angle CCD

In this subsection, the flowchart of the multi-angle CCD method proposed in this paper is shown in Fig. 4. The algorithm process is divided into two parts: single-angle difference image generation and multi-angle composed difference image generation. Some main steps of the flowchart are illustrated as follows.

(i) Geometric correction. This is a necessary step before any other processing, so that the image's projection precisely matches a specific projection surface or shape. Through this step, accurate ground projection images can be obtained.

(ii) Cross-track image registration. The registration method based on fast Fourier transform [31] is performed to achieve accurate sub-pixel registration both in range and azimuth dimensions.

(iii) Affine transform calibration. There are translation, rotation, and scaling between two single-angle difference images brought by observation perspective. In this step, affine transform based on route profile data is implemented to eliminate large position deviations.

(iv) Multi-scale image registration. The methodology used is a classic multi-scale approach [32] . These displacement vectors are found by maximizing cross-correlation metric.

(v) Multi-angle composed estimation. An incoherent composed detector is conducted by using the calibrated degree of coherence after geometric correction and registration.

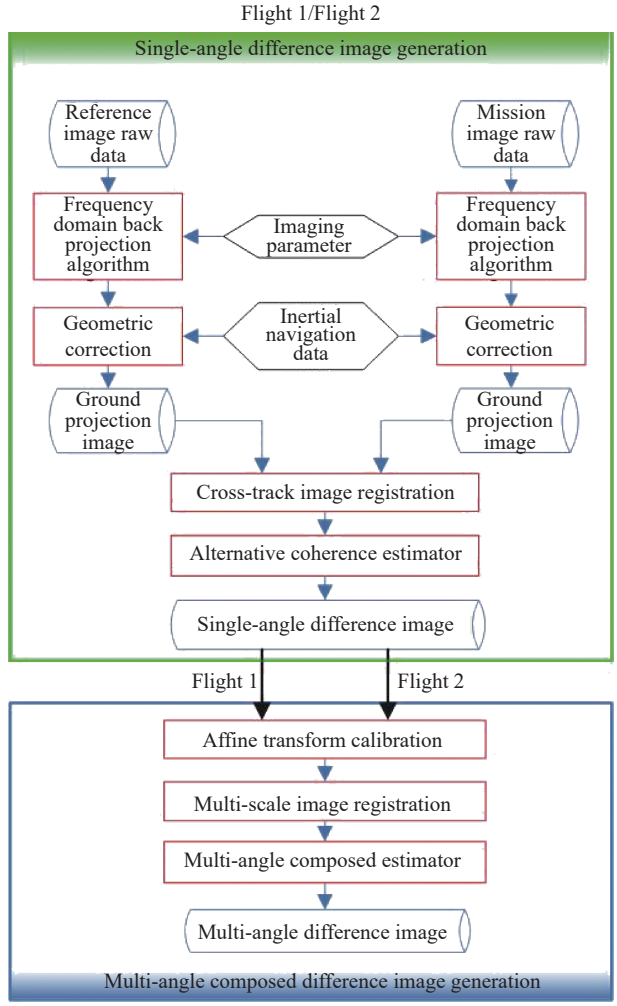

Fig. 4 Flowchart of the proposed multi-angle CCD algorithm

4. Experiments

4.1 Near-field experiments

In this subsection, a near-field experiment platform is set up in the electromagnetic spectrum laboratory to compare the performance of multi-angle CCD and single-angle CCD without the influence of environment and system. A Ka-band SAR radar is mounted on a fixed circular orbit, and a 2 m sandy platform is set in the middle of the scene as the target scenario. The experimental platform and the optical image of target scenario are shown in Fig. 5. We perform artificial footprint disturbance between two observations. The changed and unchanged scenes are determined by visual inspection and recorded as a binary mask, as shown in Fig. 6(c), which is used as ground truth to calculate the PD and the PFA for each estimator. Fig. 6(a) and Fig. 6(b) show the SAR images of the targets scenario. As can be seen from the full-angle SAR image in Fig. 6(d), due to the strong background

clutter, it is difficult to distinguish the disturbance even from the full-angle SAR image.

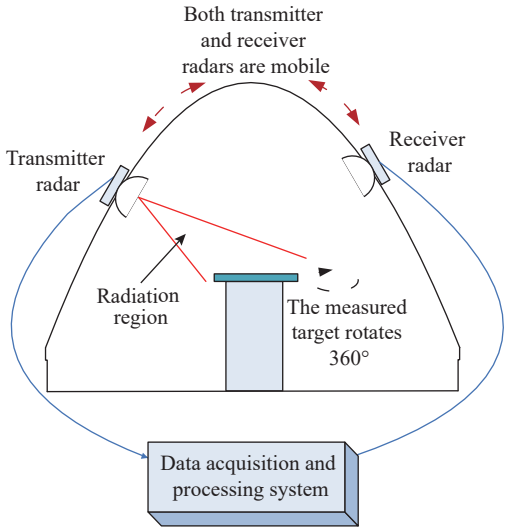

(a) System platform

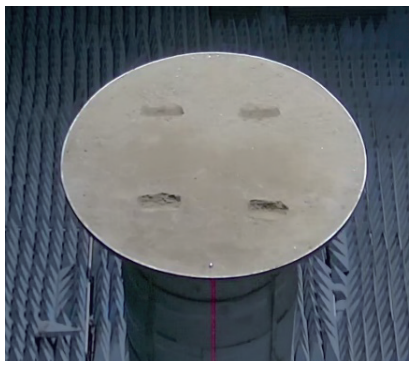

(b) Artificial footprint target

Fig. 5 Optical images of the target scenario

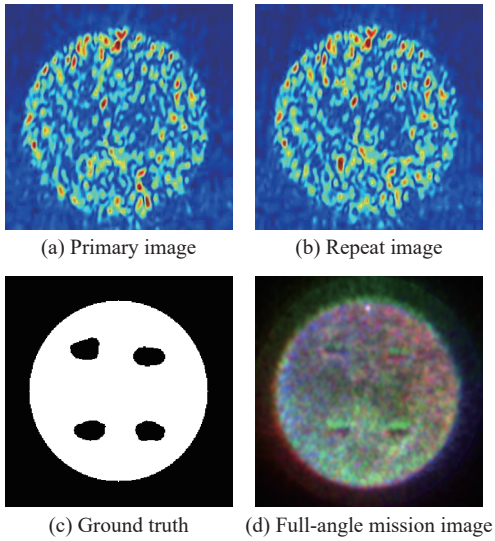

(a) Primary image (b) Repeat image

(c) Ground truth (d) Full-angle mission image

Fig. 6 Images of the targets scenario

The detection statistic chart using different number of multi-angle images with the angle interval $\theta_{\text{interval}} = 1.6°$ is shown in Fig. 7. At the same separation interval, increasing the number of composite images can reduce false alarms and obtain a clearer footprint profile.

(a) Single angle (b) Four angles (c) Ten angles

Fig. 7 Detection statistic map for $\theta_{\text{interval}} = 1.6°$

The angle intervals of 1.6° and 88° are selected for further observation as shown in Fig. 8. The number of composed images is 4. Increasing θ_{interval} can improve the performance.

(a) Single angle (b) θ_{interval}=1.6° (c) θ_{interval}=88°

Fig. 8 Four angles CCD

By observing Fig. 7 and Fig. 8, we can conclude that increasing θ_{interval} or N_{composed} can reduce the detection false alarm. A new variable called fusion angle is introduced and expressed as $\theta = \theta_{\text{interval}} \times N_{\text{composed}}$. Fig. 9 shows PD and PFA lines with the fusion angle ranging from 1° to 360° under the number of composite images $N_{\text{composed}} = 4$ and $N_{\text{composed}} = 10$. We conclude that multi-angle images have better detection results than single-angle image at a wider fusion angle. The turning point in the improvement of false alarm is $\theta \approx 25°$. Continuing to increase the fusion angle after that point provides limited performance improvement. In particular, under the same fusion angle, the performance of 10 composite images is slightly better than that of four composite images.

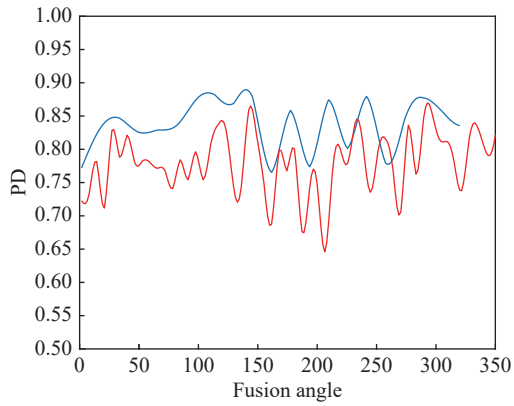

(a) PD

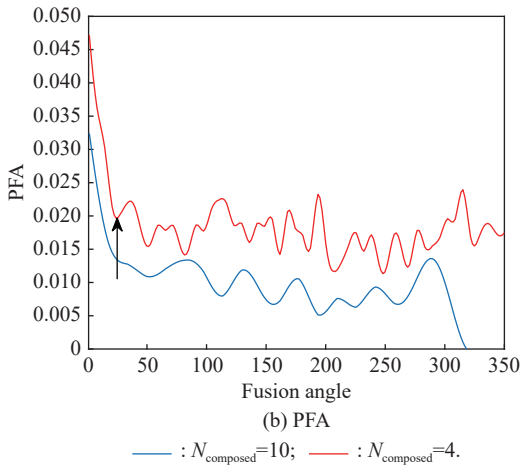

Fig. 9 The fusion angle influence

4.2 Outfield experiments

In this subsection, a Ka-band measured data experiment is given. The controlled scene change is a light wheel track using a vehicle ridden across the interested region and some footprints walk through it. The optical image is shown in Fig. 10. The landscape is hard Gobi desert, with some soil slopes and bushes across the scene. The multi-pass SAR data are acquired at an interval of 30 min. SAR images obtained by Flight 1 and Flight 2 are shown in Fig. 11(a) and Fig. 11(b). They are acquired from opposite directions. The heading angles of these two flights are 0.33° and 180.37°, which means $\theta_{interval} \approx 180°$. Single-angle CCD difference images of each flight are shown in Fig.12. The two-angle CCD image formed by the fusion method in this paper is shown in the center of Fig.13.

Fig. 10 Optical image

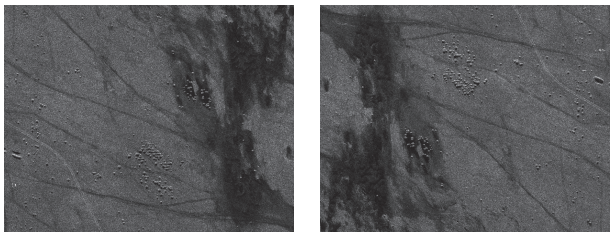

(a) Flight 1 SAR image (b) Flight 2 SAR image

Fig. 11 SAR images ($\theta_{interval} \approx 180°$)

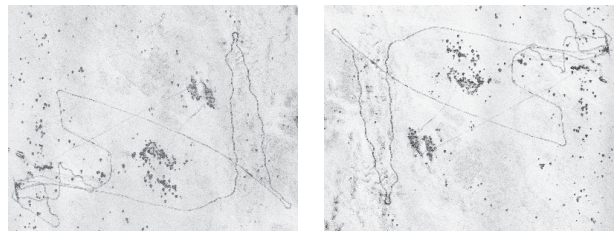

(a) Flight 1 CCD image (b) Flight 2 CCD image

Fig. 12 Single-angle CCD

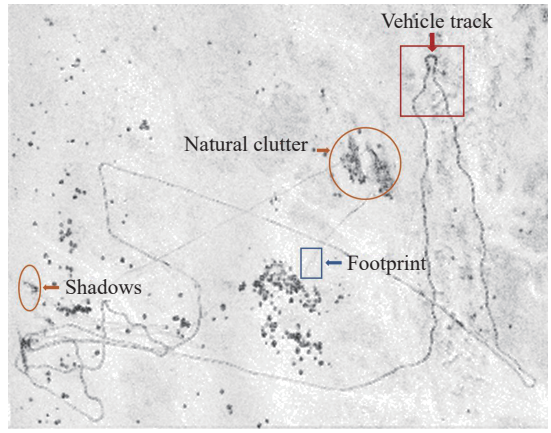

(a) Two-angle composed CCD image

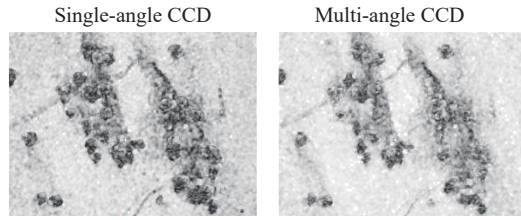

(b) Undesirable disturbance caused by bushes

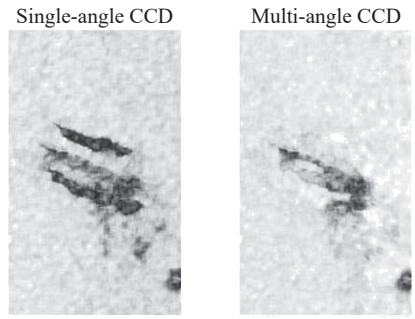

(c) Undesirable disturbance caused by shadows

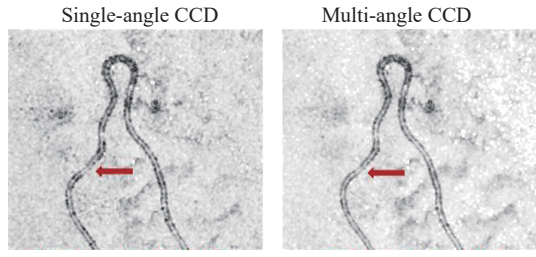

(d) Vehicle track changes

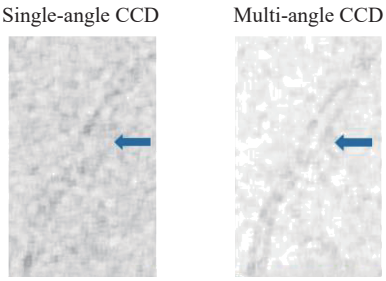

(e) Footprints changes

Fig. 13 Two-angle CCD images

As a specific example, four larger view segments of Fig. 13 are used to compare the performance of the single-angle coherence estimator and the two-angle change detector. Due to the noisy nature of SAR, we are primarily interested in low PFA, as there can be numerous uninteresting changes caused by vegetation and radar shadows. In Fig. 13, the undesirable disturbance caused by bushes and shadows of soil slopes can be reduced by the two-angle estimator. Especially, the shadow area is decreased obviously. In vehicle track detection shown in Fig. 13(d), the target contour obtained by multi-angle algorithm is more distinct, and the marks formed by two wheels are more separate. In single-angle CCD, the footprints changes are not significantly different from the false alarms. However, in multi-angle CCD, the footprint change can be clearly distinguished and represented by significantly darker pixels.

5. Conclusions

Aiming at the problem of fine traces detection, a multi-angle SAR CCD estimator is proposed to obtain a more complete fine traces description and reduce detection false alarms caused by clutter decoherence. It jointly accumulates single-angle alternative estimator results to enhance the contrast between the change target and the background clutter without a significant loss of resolution. The detection performance sensitivity to the number of composite images and the angle interval is analyzed. Experimental results show that this algorithm can improve the performance of fine change detection.

References

[1] YU Q Z, ZHANG M, YU L J, et al. SAR image change detection based on joint dictionary learning with iterative adaptive threshold optimization. IEEE Journal of Selected Topics in Applied Earth Observations and Remote Sensing, 2022, 15: 5234–5249.

[2] CRISTIAN S P, ARMANDO M, JUAN M, et al. Multitemporal polarimetric SAR change detection for crop monitoring and crop type classification. Journal of Selected Topics in Applied Earth Observations and Remote Sensing, 2021, 14: 12361–12374.

[3] ZHANG R, XIANG W, LIU G X, et al. Interferometric coherence and seasonal deformation characteristics analysis of saline soil based on Sentinel-1A time series imagery. Journal of Systems Engineering and Electronics, 2021, 32(6): 1270–1283.

[4] BRISCO B, MAHDIANPARI M, MOHAMMADIMANESH F. Hybrid compact polarimetric SAR for environmental monitoring with the RADARSAT constellation mission. Remote Sensing, 2020, 12(20): 3282–3301.

[5] GARIOUD A, VALERO S, GIORDANO S, et al. On the joint exploitation of optical and SAR imagery for Grassland monitoring. Remote Sensing, 2020, B3(XLIII): 591–598.

[6] SADRA K, MOHAMMAD G, MASASHI M, et al. A deep learning model for road damage detection after an earthquake based on synthetic aperture radar (SAR) and field datasets. IEEE Journal of Selected Topics in Applied Earth Observations and Remote Sensing, 2022, 15: 5753–5765.

[7] CORR D G. Coherent change detection for urban development monitoring. Proc. of the IEEE Colloquium on Radar Interferometry, 1997. DOI: 10.1049/ic:19970856.

[8] PREISS M, GRAY D A, STACY N J S. Detecting scene changes using synthetic aperture radar interferometry. IEEE Trans. on Geoscience and Remote Sensing, 2006, 44(8): 2041–2054.

[9] WANG M M, HUANG G M, ZHANG J X, et al. A weighted coherence estimator for SAR coherent change detection. IEEE Trans. on Geoscience and Remote Sensing, 2022, 60: 5228912.

[10] PREISS M, STACY N J S. Coherent change detection: theoretical description and experimental results. Edinburgh, Australia: Defense Science and Technology Organization, 2006.

[11] TOUGH R J A, BLACKNELL D, QUEGAN S. A statistical description of polarimetric and interferometric synthetic aperture radar. Mathematical, Physical and Engineering Science, 1995, 449(1937): 567–589.

[12] JUST D, BAMLER R. Phase statistics of interferograms with applications to synthetic aperture radar. Applied Optics, 1994, 33(20): 4361–4368.

[13] TOUZI R, LOPES A, BRUNIQUEL J, et al. Coherence estimation for SAR imagery. IEEE Trans. on Geoscience and Remote Sensing, 1999, 37(1): 135–149.

[14] BERGER T. On the correlation coefficient of a bivariate, equal variance, complex Gaussian sample. The Annals of Mathematical Statistics, 1972, 43(6): 2000–2003.

[15] MICHAEL N, GERALD B, STEPHEN K. A generalized likelihood ratio test for SAR CCD. Proc. of the 46th Asilomar Coference on Signals, System and Computers, 2012: 1727–1730.

[16] XU H P, LI Z H, LI S, et al. A nonlocal noise reduction method based on fringe frequency compensation for SAR interferogram. Journal of Selected Topics in Applied Earth Observations and Remote Sensing, 2021, 14: 9756–9767.

[17] ZHUANG H F, FAN H D, DENG K Z, et al. Change detection in SAR images based on progressive nonlocal theory. IEEE Trans. on Geoscience and Remote Sensing, 2022, 60: 5229213.

[18] DELEDALLE C A, DENIS L, TUPIN F. NL-InSAR: nonlocal interferogram estimation. IEEE Trans. on Geoscience and Remote Sensing, 2011, 49(4): 1441–1452.

[19] LIN J, HUANG Y L, PEI J F, et al. A multi-pass coherent

change detection method for SAR images in weak change circumstance. Proc. of the CIE International Conference on Radar, 2016. DOI: 10.1109/RADAR.2016.8059270.
[20] NOVAK L. Change detection for multi-polarization, multi-pass SAR. Proc. of the SPIE Conference on Algorithms for Synthetic Aperture Radar Imagery, 2005: 234–246.
[21] MONTI-GUARNIERI A V, BROVELLI M A, MANZONI M, et al. Coherent change detection for multipass SAR. IEEE Trans. on Geoscience and Remote Sensing, 2018, 56(11): 6811–6822.
[22] ZHANG Z G, SHEN W J, LIN Y, et al. Single-channel circular SAR ground moving target detection based on LRSD and adaptive threshold detector. IEEE Geoscience and Remote Sensing Letters, 2022, 19: 4505505.
[23] WEI Y K, LI Y C, CHEN X L, et al. Multi-angle SAR sparse image reconstruction with improved attributed scattering model. IEEE Geoscience and Remote Sensing Letters, 2019, 17(7): 1188–1192.
[24] EMILIANO C, ELIAS M D, DANIEL H. Multi-view 3-D radar imaging of moving targets with time-domain processing. IEEE Trans. on Geoscience and Remote Sensing, 2021, 60: 5219212.
[25] NAN Y J, HUANG X J, GUO Y J. An universal circular synthetic aperture radar. IEEE Trans. on Geoscience and Remote Sensing, 2021, 60: 5211115.
[26] ZHAO X, LIAO X, DING Z G, et al. A method for moving target detection based on airborne multi-aspect SAR system. Proc. of the IEEE International Conference on Signal Processing, Communications and Computing, 2016. DOI: 10.1109/ICSPCC.2016.7253666.
[27] OLIVER C, QUEGAN S. Understanding synthetic aperture radar images. Norwood: Artech House, 1998.
[28] CHA M, PHILLIPS R, WOLFE P J. Test statistics for synthetic aperture radar coherent change. Proc. of the IEEE Statistical Signal Processing Workshop, 2012: 5–8.
[29] CHA M, PHILLIPS R D, WOLFE P J, et al. Two-stage change detection for synthetic aperture radar. IEEE Trans. on Geoscience and Remote Sensing, 2015, 53(12): 6547–6560.
[30] CAO Z J, XU L Y, FENG J L. Automatic target recognition with joint sparse representation of heterogeneous multi-view SAR images over a locally adaptive dictionary. Signal Processing, 2016, 126: 27–34.
[31] TANG Y X, WANG C H, ZHANG H, et al. An auto-registration method for space-borne SAR images based on FFT-shift theory and correlation analysis in multi-scale scheme. Proc. of the IEEE International Geoscience and Remote Sensing Symposium, 2013: 3550–3553.
[32] PAUL H E. MREG V1.1: a multi-scale image registration algorithm for SAR applications. New Mexico, U.S. : Sandia National Lab, 2013.

Biographies

KOU Xiuli was born in 1986. She received her B.S. and M.S. degrees from Xidian University in 2009 and 2011 respectively. She is currently working toward her Ph.D. degree in signal and information processing in Beihang University, China. She is a senior engineer in Beijing Institute of Radio Measurement. Her research interests are synthetic apterture radar change detection and image interpretation.
E-mail: xiuli_kou@163.com

WANG Guanyong was born in 1989. He received his B.S. degree from Tianjin University in 2011, and M.S. and Ph.D. degrees in 2014 and 2018 respectively from the Defense Technology Academy of China Aerospace Science and Industry Corporation. He is a senior engineer in Beijing Institute of Radio Measurement. His research interests are high band synthetic aperture radar (SAR) imaging and high precision motion compensation technology such as millimeter wave SAR signal processing.
E-mail: guanbingwang@126.com

LI Jun was born in 1982. He received his B.S. and Ph.D. degrees in electrical engineering from Xidian University, Xi'an, China, in 2006 and 2011, respectively. He is a researcher with the Beijing Institute of Radio Measurement, Beijing, China. His research interests include radar system design, SAR/ISAR radar imaging and motion compensation.
E-mail: lijun_sar@sina.com.cn

CHEN Jie was born in 1973. He received his B.S. and Ph.D. degrees in information and communication engineering from Beihang University, Beijing, China, in 1996 and 2002, respectively. From 2004 to 2010, he has been an associate professor with the School of Electronics and Information Engineering, Beihang University. He was a visiting researcher with the School of Mathematics and Statistics, University of Sheffield, Sheffield, U.K., from 2009 to 2010, working on ionospheric effects on low-frequency space radars that measure forest biomass and ionospheric electron densities. Since July 2011, he has been a professor with the School of Electronics and Information Engineering, Beihang University. His research interests include multimodal remote sensing data fusion, high-resolution spaceborne synthetic aperture radar (SAR) image formation, and SAR image quality enhancement.
E-mail: chenjie@buaa.edu.cn